

A model of Titan's haze of fractal aerosols constrained by multiple observations

P. Rannou^{a,*}, C.P. McKay^b, R.D. Lorenz^c

^a*Service d'Aéronomie, B102, Université de Paris 6, 4, Place Jussieu, 75252 Paris, France*

^b*Space Science Division, NASA Ames Research Center, Moffett Field, CA 94035, USA*

^c*Lunar and Planetary Laboratory, University of Arizona, Tucson, AZ 85721, USA*

Received 29 October 2002; received in revised form 7 May 2003; accepted 12 May 2003

Abstract

We use Titan's geometric albedo to constrain the vertical distribution of the haze. Microphysical models incorporating fractal aggregates do not readily fit the methane features at 0.62 μm band and the dark 0.88 μm of the albedo spectrum simultaneously. We take advantage of this apparent discrepancy to constrain the haze vertical profile.

We used the geometric albedo and several results and constraints from other works to better constrain the vertical haze extinction profile, especially in the low stratosphere. The objective of this model is to give a solution that simultaneously fits the main constraints known to apply to the haze.

We find that the haze extinction increases with decreasing altitude with a scale height about equal to the atmospheric scale height down to 100 km. Below this altitude, extinction must decrease down to 30 km. This is necessary in order to have enough haze to sustain a relatively high albedo (0.076) in the dark 0.88 μm methane band and to show the 0.62 μm band in the haze continuum. We set the haze production rate around $7 \times 10^{-14} \text{ kg m}^{-2} \text{ s}^{-1}$, and the aerosols production altitude around 400 km (or at pressure 1.5 Pa).

The physical processes which generate such a profile are not clear. However, purely one-dimensional effects such as condensation, sedimentation, and rainout can be ruled out, and we believe that this relative clearing in Titan's troposphere and lower stratosphere is due to particle horizontal transport by the mean circulation.

© 2003 Elsevier Ltd. All rights reserved.

Keywords: Titan; Atmosphere structure; Photometry; Haze

1. Introduction

The atmosphere of Titan contains an organic haze that is optically thick at visible wavelengths. The geometric albedo of Titan as a function of wavelength provides a useful data set for comparing to microphysical and radiative models of this haze. McKay et al. (1989) used a simple analytic microphysics model and treated the haze particles as compact spheres. They were able to fit the geometric albedo from the visible to the near-infrared and showed that the geometric albedo depended on the surface reflectivity as well as the optical properties, electrical charge, and production rate of the haze. They found that the geometric albedo could be fit assuming that the optical properties of the haze were scaled

in the visible by a factor of 4/3 to the laboratory measurements of Titan tholin (Khare et al., 1984). Courtin et al. (1991) found that this spherical model did not match the geometric albedo in the UV unless a second mode of small spherical particles ($< 10 \text{ nm}$) were added. Toon et al. (1992) developed a complete microphysics model of the haze and included diffusion—important in the lower atmosphere—and vertical winds. They were able to match the UV spectrum with small particles high in the atmosphere carried upward by diffusion and vertical motions. The detached limb feature of the haze could be generated by vertical motions of order 1 cm/s.

Spacecraft data have also suggested that there were two modes of particles in Titan's upper atmosphere (Tomasko and Smith, 1982). Data from Pioneer 11 and Voyager photopolarimetry (Tomasko and Smith, 1982; West et al., 1983) showed large positive polarization at $\sim 90^\circ$ phase angle. This requires particles, if spherical in shape, with radii no

* Corresponding author. Tel.: +33-1-4427-4970; fax: +33-1-4427-3776.

E-mail address: pra@ccr.jussieu.fr (P. Rannou).

larger than 0.1 μm . However, Voyager observations (Rages et al., 1983) of the brightness of Titan at high phase angles require particles that are at least 0.2 μm and probably 0.5 μm in radius.

An explanation, alternative to the bi-modal distribution of spherical particles proposed by Courtin et al. (1991) and Toon et al. (1992), are fractal aggregates of spherical ‘monomers’, proposed by West and Smith (1991). In a series of papers Cabane and coworkers (Israel et al., 1991; Cabane et al., 1992, 1993; Chassefière and Cabane, 1995; Rannou et al., 1993, 1995, 1997) have developed a sophisticated model of Titan’s haze based on fractal particles. A similar model has been developed by Tomasko et al. (1997).

The basis for fractal models lies in the observation that when liquid particles combine they form a new compact sphere corresponding to the combined mass, but when solid particles combine they can form a range of shapes from compact spheres to long strings of particles. Previous microphysical models (Cabane et al., 1992, 1993) suggest that Titan’s main haze can be physically divided into two regions, a high altitude region in which the fractal dimension is 3 (monomer growth) and a lower altitude region in which the fractal dimension is 2 (cluster–cluster ballistic growth). Fractal particles behave optically like a bi-modal distribution of spherical particles (West, 1991). The small particles, both the free monomers and the monomers within aggregates, interact with short wavelength radiation and also determine the polarization. Thus the UV and polarization data can be explained. At longer wavelengths the aggregates behave like large particles and can reproduce the geometric albedo and forward scattering properties observed for Titan (Botet et al., 1997; Rannou et al., 1999).

However fractal models have one difficulty not present in the spherical models. That is the important methane feature at 0.62 μm , appearing in the spectrum, is not fit by the fractal model. In particular the fractal haze is optically thicker than models of spherical aerosols in the atmosphere at these wavelengths and the photons that are reflected do not pass through enough gas to create the methane absorption feature observed in the geometric albedo spectrum.

Tomasko et al. (1997) have obtained a fit to the 0.62 μm band by removing the haze for altitudes below 90 km (see Fig. 7 of Tomasko et al., 1997, also shown as Fig. 6 of McKay et al., 2001). However this model is not well developed and the implications and constraints of this fitting approach are not discussed. In this paper we carefully examine the implications for the 0.62 μm feature for fractal haze models and consider the extent of clearing of the haze in the lower atmosphere that is required to fit the geometric albedo at this wavelength. We compare our results to the recent suggestion by Young et al. (2002) based on multispectral HST data that there is a haze clearing in Titan’s lower atmosphere (see also Chanover et al., 2003). We also briefly consider possible explanations for this haze clearing.

2. Light in the troposphere

Fig. 1 shows a comparison of the total vertical optical depth in the McKay et al. (1989) and Toon et al. (1992) spherical models and the fractal models of Rannou et al. (1997) and Tomasko et al. (1997). Also shown are the recent determinations of haze optical depth by Young et al. (2002), Gibbard et al. (1999), and Griffith et al. (1991). Fig. 1 illustrates the basic difference between the spherical and fractal models and the source of the problem for the fit of the fractal models at 0.62 μm . Fractal particles in Titan’s atmosphere are fluffy (fractal dimension near 2). They scatter light in a different way than spherical aerosols. This generates a large total optical depth in the visible and UV (the wavelengths at which the fractal particles are efficient absorbers,) which obscures the methane feature at 0.62 μm . However in a scattering atmosphere the extinction optical depth shown in Fig. 1 is not a useful estimate of the penetration of photons into the atmosphere. A more useful parameter is the effective optical depth (or effective opacity) τ^* given by (e.g., Pollack and McKay, 1985)

$$\tau^* = \tau \sqrt{(1 - \omega)(1 - \omega g)}, \quad (1)$$

where ω is the single scattering albedo and g is the asymmetry factor (the mean value of scattering angle cosine

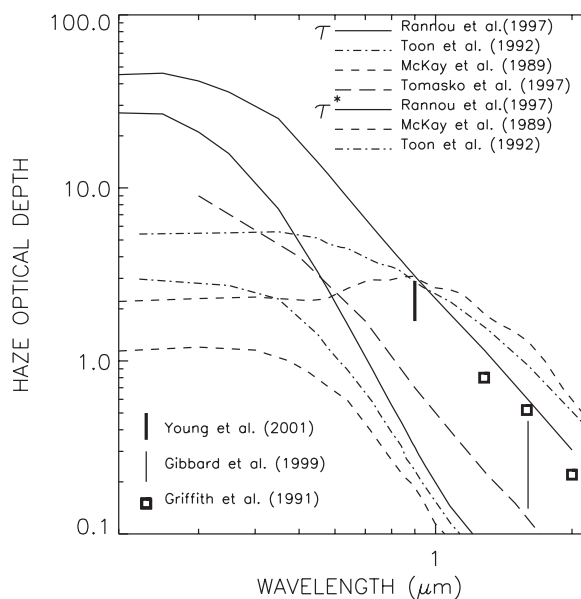


Fig. 1. The integrated haze optical depth as a function of wavelength for McKay et al. (1989) and Toon et al. (1992) models of spherical aerosols (dashed thick line and dot-dashed thick line, respectively) and for the fractal aggregates model based on Rannou et al. (1995) (thick continuous line) and Tomasko et al. (1997) (thick dotted line). The thin dot-dashed line and thin continuous lines correspond to the effective haze opacity for Toon et al. (1992) and Rannou et al. (1995) as explained in the text. Values retrieved from near-infrared data are also plotted for comparison (vertical line at 0.9 μm : Young et al., 2002, vertical lines at 1.6 and 2.1 μm : Gibbard et al., 1999, empty bold squares: Griffith et al., 1991).

weighted by the phase function; $g=0$ for a symmetric phase function such as for Rayleigh scattering and g increases toward 1 for a strongly forward scattering as for large particle). This relation accounts for the fact that some of the scattered photons continue downward and are not lost from the downward flux as rapidly as the total extinction optical depth would imply if there was no scattering present. Fig. 1 also shows a comparison of the total vertical effective optical depth (thin line) for Rannou et al. (1997), McKay et al. (1989) and Toon et al. (1992). In the following, effective optical depth or effective opacity will be shown as τ^* , and optical depth or opacity will be shown as τ .

For the methane feature at $0.62 \mu\text{m}$ to be visible, the effective optical depth must be less than 2 so that the photons pass through the tropospheric methane. As seen in Fig. 1, this is not the case for the reference fractal model or Rannou et al. (1997). Toon et al. (1992) succeed in fitting the albedo with spherical aerosols because the UV is obscured by particles which are lifted at high altitude. However their model does not account for all the observational constraints. Particularly, the aerosol mean radius in the main haze layer is set to about $0.1 \mu\text{m}$. This is consistent with West et al. (1983) polarimetry but not with Rages and Pollack (1983) high phase angle polarimetry. These two data sets actually yield discrepant estimates of aerosol radius for the same part of the haze, but this was solved by considering aggregates.

For this work, we use a composite set of several measurements for the geometric albedo. The UV part ($0.2\text{--}0.4 \mu\text{m}$) is a measurement of IUE (Courtin et al., 1991). Visible and near-infrared data ($0.4\text{--}1 \mu\text{m}$) are from Neff et al. (1984) and the five data points in the near-infrared between 0.94 and $2.0 \mu\text{m}$ are from Coustenis et al. (1995). In Fig. 2, the $0.62 \mu\text{m}$ band (the shortest wavelength prominent band) is partially masked by haze scattering. For this reason, it gives important information on the respective role of haze and methane down to the troposphere. The $0.88 \mu\text{m}$ bands is one of the strongest band of the spectrum below $1 \mu\text{m}$, and is known to depend on an altitude range well above tropopause.

3. The haze model

In this part, we briefly describe the haze microphysical model, and we present the important parameters relative to the microphysics and the optics of particles. We also describe the role of the eddy diffusion coefficient on the vertical structure of the haze and especially on the vertical extinction profile.

3.1. The microphysics

We have developed an analytic microphysical model based on the approach of McKay et al. (1989). Our motivation is that full microphysical models such as Toon et al. (1980) or Cabane et al. (1992) are generally complex. They deal with a fully described aerosol distribution and

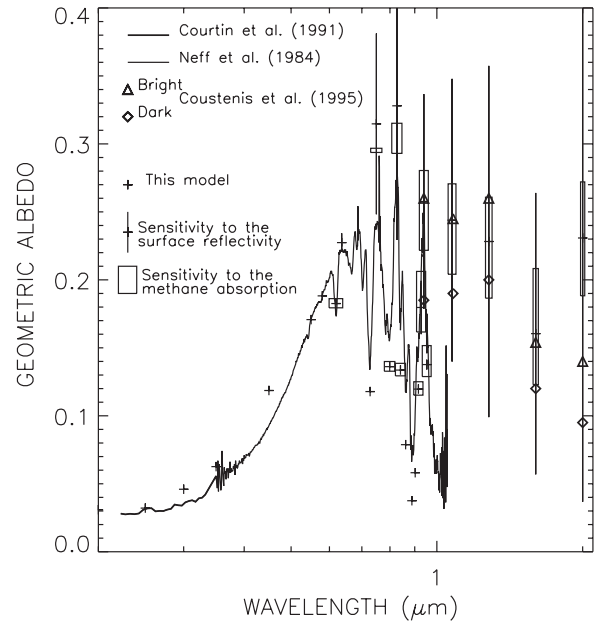


Fig. 2. The observed geometric albedo in UV (Courtin et al., 1991), in visible ($0.35\text{--}1 \mu\text{m}$) (Neff et al., 1984), and near-infrared (Coustenis et al., 1995). A fit is also shown for a case without cut-off (see also Table 1). The thin vertical lines show the sensitivity of the fit when the surface reflectivity is varied from 0 to 1. The boxes show the sensitivity of the fit to the uncertainties on the methane extinction coefficient (see the text for details).

solve numerically the microphysical equations, including coagulation, coalescence, sedimentation and eddy diffusion. Such models, called eulerian models, can be used to find the time dependent evolution of a haze distribution. They are powerful tools for aerosol science.

The drawback is that they run slowly. For Titan studies, one generally needs a converged steady state solution. Because aerosols fall in some 100 terrestrial years (Rannou et al., 1993) the eulerian models are not convenient for intensive use, such as investigating a multi-dimensional space of microphysical parameters.

The idea of the present model is to develop a simple analytical solution of the aerosol growth and settling. The differential equation to solve (Eq. (A.9) in Appendix A) links the aerosol radius to the altitude in the atmosphere. The aerosol density is then deduced from the settling speed and the mass flux conservation. Thus, the model yields the aerosol size and density as a function of altitude, assuming a steady state convergence.

The model solves the equation in two steps. In the production zone, aerosols grow spherically since the aerosol distribution is thought to be polydispersed. When aerosols fall below the production zone, the individual spherical particles (called monomers here) are all approximately the same size but they begin to form fractal structures (Cabane et al., 1992). Thus, the monomer radius is self-consistently computed in the model based on condi-

tions in the production zone. To deal with formation of fractal aggregates, we have modified the microphysical laws following Cabane et al. (1993), and we have added eddy diffusion, a process that was not included in the original McKay et al. (1989) model. Eddy diffusion has been used in almost all previous works, but with widely different diffusion coefficients. Eddy diffusion can profoundly affect the microphysical solution. We discuss this aspect in the next paragraph, and we suggest a constraint on this parameter.

The details of the microphysical model as well as its performance are compared to the reference eulerian model (e.g. Cabane et al., 1992, 1993) in Appendix A. We also show that the haze optical properties which are derived from our model are in good agreement with previous radiative transfer models (Rannou et al., 1997).

3.2. Parameters of the model

The main parameters of the microphysical model are the haze production rate Q , the haze production pressure, the aerosol charging rate χ , and the eddy diffusion coefficient, K . These parameters define the aerosol distribution. For the geometric albedo, three more parameters are the aerosol imaginary refractive index $n_i(\lambda)$, the ground reflectivity R_s and the methane absorption coefficient k_{CH_4} . With these seven parameters, the geometric albedo due to the haze, the atmosphere and the surface is well defined.

To deal with convenient parameters, we use relative factors for the haze production rate, P_0 which is defined as $P_0 = Q/Q_{\text{ref}}$, where $Q_{\text{ref}} = 3.5 \times 10^{-13} \text{ kg m}^{-2} \text{ s}^{-1}$, for the eddy diffusion coefficient defined as $\kappa = K/K_{\text{ref}}$ where K_{ref} is the profile used in Cabane et al. (1992) and for the imaginary refractive index, $X_k = n_i(\lambda)/n_{i\text{ref}}(\lambda)$ where $n_{i\text{ref}}(\lambda)$ is the imaginary part of the refractive index given by Khare et al. (1984). We also use the real part of the refractive index published by Khare et al. (1984). Methane extinction coefficient are taken from Karkoschka (1994) below 1 μm and are those used by Coustenis et al. (1995) between 1 and 2 μm . In this model, we account for Rayleigh scattering by atmosphere.

We also want to encompass the uncertainties on the surface reflectivity and the methane absorption. Thus we consider cases with the surface reflectivity R_s set successively to 0 and 1, and for the methane absorption set to its extremal values. Following Karkoschka (1994), we considered an uncertainty of 20% for the 0.62 μm band ($k = 0.6 \text{ km-am}^{-1}$) and 50% on the near-infrared methane band extinction values ($k \simeq 0.05 \text{ km-am}^{-1}$) as suggested by Coustenis et al. (1995). For other values, we use a linear interpolation and extrapolation of the uncertainty ratio versus $\log(k)$. This approach provides an estimate of the extent to which the uncertainties on the methane extinction coefficient modify the fits. In Fig. 2 this uncertainty in methane extinction appears as uncertainty boxes on the computed albedo. Un-

certainities due to surface reflectivity appear as vertical bars, showing the albedo computed using the two extreme values for R_s .

3.3. Effect of the diffusion coefficient

The vertical structure of the haze is partly defined by the microphysics, which is basically well known. However, eddy diffusion, which in a sense represents the action of the atmospheric motions on the haze, can profoundly modify the purely microphysical solution. In general, eddy diffusion accelerates the downward transport of aerosols and, depending on its intensity, may dominate sedimentation. When this happens, eddy diffusion determines the scale height of the vertical profile. This is particularly true when dealing with slowly falling particles like fractal aggregates. Among the 1D models which have been published, many eddy diffusion coefficients have been used. They are generally based on simple physical arguments for the general shape of the profile, at least in the stratosphere. The strength of the coefficients are either ad-hoc or roughly estimated. That leads to a variety of the eddy coefficient profiles with a factor 10 between the two extreme cases. The shapes also vary in the low stratosphere and in the troposphere. If the eddy diffusion coefficient is larger than the values used by Yung et al. (1984) profile, then the haze distribution is essentially driven by diffusion.

We have used the same stratospheric eddy diffusion profile as Cabane et al. (1992) scaled by a factor, κ , between 0 and 1.4, to test the sensitivity of the extinction vertical profile in our model. The eddy diffusion, as generally parameterized in 1-D models, particularly affects the extinction profile below 250 km by increasing the scale height of the haze. As the scale height of the haze increases in the troposphere the total optical depth between the optical depth unity level of the haze in the stratosphere and the surface decreases. Thus for a given haze production rate, the larger is the eddy diffusion coefficient, the lower is the integrated opacity. Thus, we can already foresee that fitting the geometric albedo with our model will require larger aerosol production rates for larger eddy diffusion coefficients.

4. Fit of the geometric albedo

In this part, we first specify the conditions that define a good fit of the geometric albedo. Then, with this set of rules, we investigate the parameter range which gives good fits. We first establish the range for haze production rate and for the eddy diffusion factor κ which is consistent with observation. These ranges implicitly include uncertainties on aerosol radius at 200 km and on monomer radius given elsewhere. In a next step, we consider additional information concerning the haze extinction at 200 km and the eddy diffusion to provide a realistic vertical haze structure.

Table 1
Main parameters of the main haze layer

| | Main haze reference parameter | |
|---------------------|--|---|
| | W/o cut-off | With cut-off |
| Production rate | $P_0 = 0.18^a$ | $P_0 = 0.23^a$ |
| Production pressure | 1.5 Pa ($\simeq 400$ km) | 1.5 Pa |
| Charging rate | $\chi = 20e^{-\mu\text{m}^{-1}}$ | $\chi = 20e^{-\mu\text{m}^{-1}}$ |
| Eddy diffusion | $\kappa = 0$ | $\kappa = 0$ |
| Refractive index | $n = n$ (Khare et al., 1984) $k = X_v \times k$ (Khare et al., 1984) $X_v = 2.0$ | |
| Haze cut-off | | $X_v = 2.3$ $Z_{\text{co}} \simeq 95$ km extinction inversion between 95 and 40 km |
| Methane profile | $x_{\text{CH}_4} = 8\%$ at the ground $S = 100\%$ in the troposphere $x_{\text{CH}_4} = 1.5\%$ at the cold trap $x_{\text{CH}_4} = 1.5\%$ in stratosphere | |

^a $\times 3.5 \times 10^{-13} \text{ kg m}^{-2} \text{ s}^{-1}$.

4.1. Qualitative and quantitative control of the fits

To quantify a fit, we essentially focus on the ability of the model to fit the $0.62 \mu\text{m}$ band and the $0.88 \mu\text{m}$. It is quite straightforward to choose a production rate which will fit the $0.62 \mu\text{m}$ band, the haze continuum, and the methane windows. However, the $0.88 \mu\text{m}$ band is systematically too dark. Fig. 2 shows an example of a fit that we obtained with our reference model as defined in Table 1 (left column). Note that the sensitivity to the surface albedo and the methane absorption are shown in Fig. 2. This fit is representative of the agreement we generally reach with the model, whatever the chosen value of κ . This means that the amount of methane which is needed to fit the $0.62 \mu\text{m}$ is too low to hide the $0.88 \mu\text{m}$ band. This apparent discrepancy appears whatever the parameters we used.

Thus, to decide if a fit is good, we check several features. First, the $0.62 \mu\text{m}$ band must be apparent and not lost in the continuum. That is, the albedo at $0.62 \mu\text{m}$ must be lower than the albedo at $0.58 \mu\text{m}$. Second, the haze continuum from 0.2 to about 0.7 have the same slope as observed. This can be easily controlled through the UV, which must be dark (around $A = 0.03$), and the visible must be at $A = 0.2$ at $0.58 \mu\text{m}$, within 10% . Third, the methane bands for $0.7 < \lambda < 0.8 \mu\text{m}$ must be well marked, with the correct geometric albedo inside the uncertainty boxes due to methane extinction uncertainties. The near-infrared albedo in the methane windows must be included in the error bars given by the extreme values of the surface reflectivity, that is R_s between 0 and 1 .

These rules, which are used in the next part, exclude the $0.88 \mu\text{m}$ methane band. We thus already know that another scattering species will be needed to increase the albedo in the $0.88 \mu\text{m}$. We will discuss this point further below. For now, fitting the albedo within the requirements as listed

above will already constrain all the parameters in the model over the ranges listed above. Additional information would be needed to further constraint the fit.

4.2. A priori constraints on the haze parameters

In this part, we first investigate the model parameters needed to correctly fit the geometric albedo. We choose to work with four values of κ which are 0 , 0.2 , 0.5 and 1 . $\kappa = 0$ corresponds to no diffusion at all, $\kappa = 0.2$ is equivalent to the Toublanc et al. (1995) profile and $\kappa = 1$ corresponds to the Cabane et al. (1992) profile. We also consider an intermediate case $\kappa = 0.5$. For each values of κ , we seek production rates Q which fit the geometric albedo. The parameters of the model are constrained by two conditions which pertain to the aerosol structure. First, the radius of aerosols at 200 km must be within in the range 0.2 – $0.5 \mu\text{m}$, defined by Rages et al. (1983). This constraint is derived from high phase angle photometry which depends on the apparent size of the particles. Thus we reject cases for which the apparent radius of the aerosols are not within this interval. The second constraint is the monomer radius. West and Smith (1991), and Tomasko et al. (1997), have studied polarimetric data from Voyager. They exclude monomer radius as small as $0.02 \mu\text{m}$ but allow $0.06 \mu\text{m}$. Large phase angle photometry also leads to monomer radius between 0.045 and $0.095 \mu\text{m}$ (Rannou et al., 1997). In this work, we allow the monomer radius to be between $\simeq 0.04$ and $\simeq 0.095 \mu\text{m}$.

It is noteworthy that the haze properties primarily depend on the monomer radius, not on the apparent size of the aggregates. The reason is that aggregate cross-sections are nearly linear with the monomer number, and the asymmetry parameters are quite constant, at least in the wavelength range that we consider. Thus haze properties do not change a lot if the apparent size of aggregates varies but the monomer radius stays fixed. On the other hand, variations of monomer radius produce significant changes in haze properties.

4.3. Constraints due to geometric albedo

Considering these limitations, for the different values of κ , we seek the possible haze production rate P_0 which will give the best fit. Fig. 3 shows the upper and lower values of P_0 as a function of the eddy diffusion case κ , for several values of the monomer radius (labeled curves). For a given monomer radius, the upper limit is fixed by the $0.62 \mu\text{m}$ band, which is hidden if the production rate becomes too large, and the lower limit is set by the requirement that UV Rayleigh scattering not dominate albedo at short wavelengths. We see that the larger is the monomer radius, the smaller is the domain which gives a good fit. For a monomer radius larger than about $0.075 \mu\text{m}$, no solution could be found. If we gather all the possibilities regardless of the monomer radius, we get that production rate P_0 may be between 0.05 and 0.90

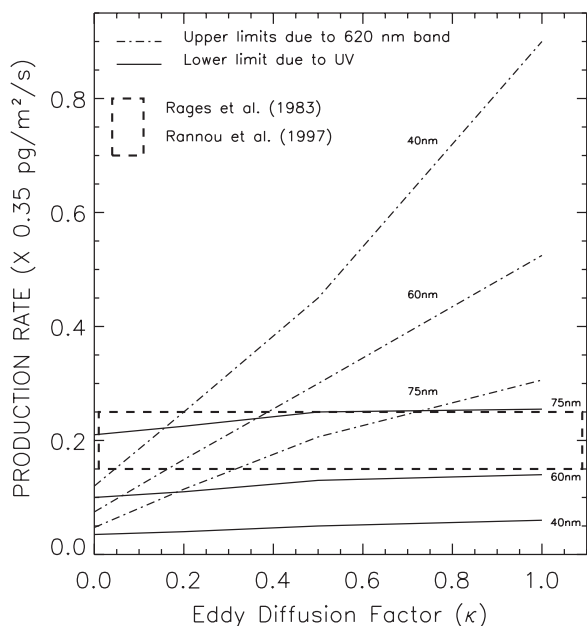


Fig. 3. The dot-dashed lines show the upper limit of the production rate beyond which the $0.62 \mu\text{m}$ band cannot appear on the geometric albedo, as a function of κ (eddy diffusion factor), for several values of the monomer radius labeled in nm. The continuous lines show the lower limit below which Rayleigh scattering begins to affect the UV albedo. Then, for a given monomer radius, only solutions above the continue line and below the dot-dashed line can fit the geometric albedo. The dashed box shows the production rate between 0.2 ± 0.05 which is derived from Voyager 1 high phase angle photometry analysis (Rages and Pollack, 1983; Rannou et al., 1997). This restrict the domain of solution and discard monomer radius larger than 75 nm.

for $\kappa = 1$, in the range 0.05–0.45 for $\kappa = 0.5$, in the range 0.04–0.25 for $\kappa = 0.2$ and in the range 0.035–0.12 for $\kappa = 0$ (Fig. 3). These ranges are essentially bounded by the range for the lower monomer radius $r_m = 0.04 \mu\text{m}$ which generally includes the range for other monomer radius cases within it.

X_k is also strongly correlated to the monomer radius, regardless of the values of κ , χ , P_0 or Q . For $r_m \simeq 0.04 \mu\text{m}$, we need $X_k \simeq 1.3$, for $r_m \simeq 0.06 \mu\text{m}$, we need $X_k \simeq 2.1$, and for $r_m \simeq 0.07 \mu\text{m}$, X_k must be set to $\simeq 2.5$. Thus, X_k is not really a free parameter.

Fig. 2 shows a typical fit that we obtain with this haze model. For each of these fits, the most important features are reproduced and the albedo sensitivity for the surface reflectivity between 0 and 1 is shown by the thin vertical lines. The boxes indicate in which extent the uncertainty on methane absorption coefficient can affect the fit. This haze model is transparent in the near-infrared. Fig. 2 also suggests that the haze is sufficiently transparent at wavelengths as short as $0.75 \mu\text{m}$ to be sensitive to surface heterogeneities. In fact, this point depends on the actual structure of the haze below the tropopause and on the thickness of possible tropospheric clouds.

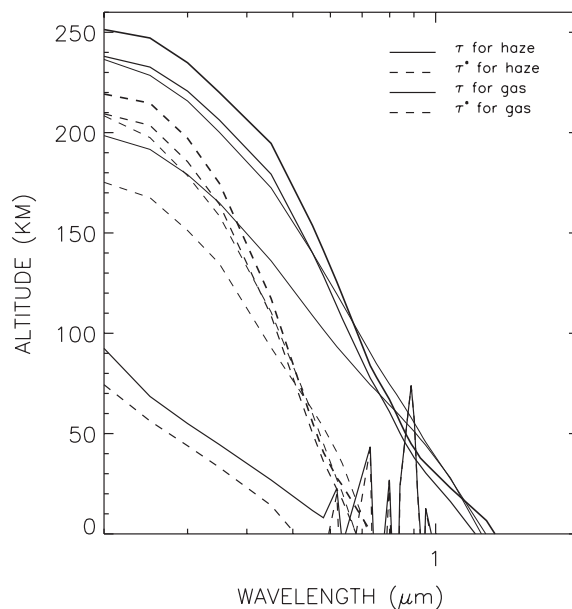


Fig. 4. The altitude for which τ (continuous line) and τ^* (dashed lines) are equal to 1. The 2 lower thin curves are for atmosphere alone (methane + nitrogen) and the two upper set of four curves are for haze only. The haze layers are set, with various values of κ , to fit the geometric albedo. The increasing thickness of the lines indicate increasing values of κ : 0, 0.2, 0.5 and 1.

4.4. Penetration of light in the atmosphere

We define $Z_1(\lambda)$ as the altitude where the unity optical depth $\tau = 1$ is reached as a function of λ . In Fig. 4, we plot $Z_1(\lambda)$ for haze alone with the four values of κ , and for the atmospheric component alone as well. As noted in the introduction, the optical depth concerns the extinction of the direct solar light, and it does not account for the fact that light is scattered and may continue its way downward. We also define the altitude Z_1^* where $\tau^* = 1$.

We first note that the altitude $Z_1(\lambda)$, as well as $Z_1^*(\lambda)$, have roughly the same behavior with wavelength whatever κ . This is not surprising since to obtain the same albedo in the methane bands, the haze efficiency has to be the same in each case. Fig. 4 indicates that the $0.62 \mu\text{m}$ band is partly hidden from outside because τ^* just reaches unity at about 30 km. There is a strong competitive effect between haze and methane for this band. On the other hand, the $0.88 \mu\text{m}$ band appears much more marked because the haze has a low effective opacity at this wavelength, and the methane absorption is strong. The level $\tau = 1$ due to methane absorption occurs around 70 km at $0.88 \mu\text{m}$. Therefore, the methane absorption largely dominates the albedo. The resulting albedo is very dark, and its exact value depends on the haze component above 70 km. In other parts of the spectrum, the geometric albedo is quite easily fit. Where methane absorption is weak, haze is the only component acting on the albedo shortward of $\simeq 0.6 \mu\text{m}$ and haze plus surface act on the albedo longward of $\simeq 0.6 \mu\text{m}$.

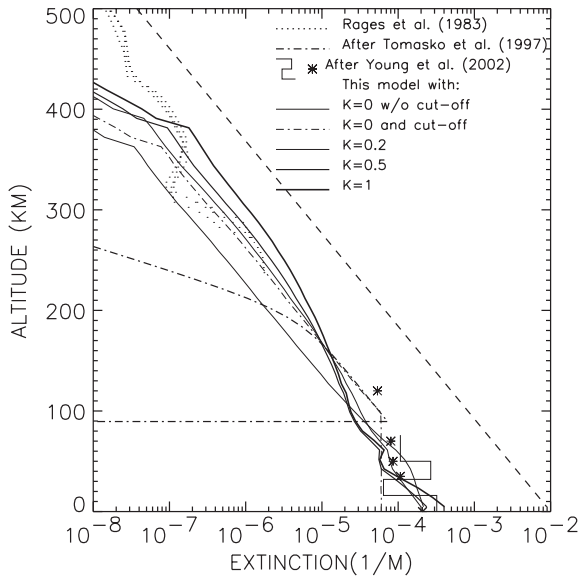


Fig. 5. Several vertical extinction profiles at $0.5 \mu\text{m}$. The three dotted line profiles are Rages and Pollack (1983) profiles for latitudes between 15°S and 15°N . The asterisks are the extinction profile at $0.5 \mu\text{m}$ derived from Young et al. (2002). The five extinction profiles starting at 500 km are for this model and for various values of κ (see legend). As explained in the text, and on Fig. 3, the larger κ , the larger must be the production rate, and thus the extinction at 200 km. The thin dot-dashed profile is derived from Tomasko et al. (1997). The dashed line at the right-hand side shows the scale height law for $H = 40 \text{ km}$.

Our results in this regard are similar to those of McKay et al. (1989) and Toon et al. (1992) for the case of spherical particles.

4.5. Additional constraint on the extinction at 200 km

With the geometric albedo alone, it is difficult to further limit the range of parameters. Therefore, we now consider results obtained from the interpretation of the high phase angle photometry (Rages and Pollack, 1983; Rannou et al., 1997). This type of data can give valuable constraints on the local haze properties between 150 and 250 km. Rages and Pollack (1983) have retrieved constraints on the vertical extinction structure above 200 km. Haze extinction coefficients from Rages et al. (1983) are plotted in Fig. 5. Rannou et al. (1997) require $P_0 \simeq 0.2 \pm 0.05$ to fit the intensity profiles. This estimate is independent of the actual monomer radius, at least between $r_m = 0.04$ and $0.11 \mu\text{m}$. It is also independent of the eddy diffusion which was used since diffusion only affects haze distribution in the lower stratosphere (below about 200 km as shown in Fig. 12). Thus, haze production rates around 0.2 should be suitable to match both the high phase angle photometry and the geometric albedo. This value from Rannou et al. (1997) is used in this work. This cannot be used to limit values of κ , except those larger than $\simeq 1$ which correspond to large haze production rates (Fig. 3).

4.6. Haze cut-off in stratosphere

At this point, it seems that the most realistic case for Titan is a haze production rate around $P_0 = 0.2$. Fig. 3 shows that $\kappa = 0$ is not consistent with $P_0 = 0.2 \pm 0.05$ but is consistent with a smaller production rate. On the other hand, models with $\kappa > 0.05$ are consistent with the constraint on P_0 .

To reconcile the fact that κ may be equal to zero and that $P_0 = 0.2 \pm 0.05$, we can introduce a cut-off in the vertical haze profile. The principle is to partially remove aerosols below a given altitude in order to decrease the total amount of haze for a given production rate. A simple haze cut-off is obtained assuming that below an altitude Z_{co} , the haze extinction is constant. With this cut-off, we find a fit with $P_0 = 0.2 \pm 0.05$ and $\kappa = 0$ simultaneously. This is possible because with the cut-off, the haze total opacity for $P_0 = 0.2$ is smaller than without the cut-off, as shown in Fig. 3.

We find that for small monomer radius ($r_m = 0.04 \mu\text{m}$), the cut off must be set above 110 km. If ($r_m = 0.06 \mu\text{m}$), the cut-off must be set above about 80 km. For large monomer radius ($r_m > 0.075 \mu\text{m}$), no solution can be found because Rayleigh scattering by the atmosphere dominates in the UV for P about $\simeq 0.2$.

As shown in Fig. 3, a solution with $P_0 = 0.2 \pm 0.05$ may also be found without invoking a cut-off for $\kappa > 0.05$. Thus a cut-off is not compulsory at this stage provided the value of κ is larger than 0.05. Moreover, a cut-off does not solve the problem with the $0.88 \mu\text{m}$ band which is still too dark.

4.7. Haze inversion profile in stratosphere

Up to now, we have excluded from our considerations the $0.88 \mu\text{m}$ feature. Previous solutions fit the geometric albedo, with the exception of this band as explained above (see Fig. 2). The simple cut-off with constant extinction below an altitude Z_{co} does not solve this problem. We now must go one step further: haze layers fitting the $0.62 \mu\text{m}$ band are not thick enough at $0.88 \mu\text{m}$, as explained above. But the $0.62 \mu\text{m}$ band is formed at an altitude $\simeq 30 \text{ km}$, whereas the $0.88 \mu\text{m}$ is formed at $\simeq 80 \text{ km}$ (Fig. 4). Thus using extinction profiles which increase with decreasing altitudes (as generally occurs in 1D models) it is impossible to increase opacity above 80 km without increasing much more opacity below (e.g., 30 km). This is the problem we must solve.

We may solve the geometric albedo problem, and especially the fit of the $0.88 \mu\text{m}$, if we could increase the opacity above about 70 km, with a moderate (or no) increase of opacity above 30 km. We could achieve this if we could transfer part of the opacity between 30 and 80 km above 80 km.

This solution means that the haze extinction must decrease below an altitude Z_{co} . To act on the $0.88 \mu\text{m}$ band albedo, Z_{co} must be at least higher than $\simeq 80 \text{ km}$. This obviously does not correspond to the general solution of one-dimensional microphysics. However, Titan haze is

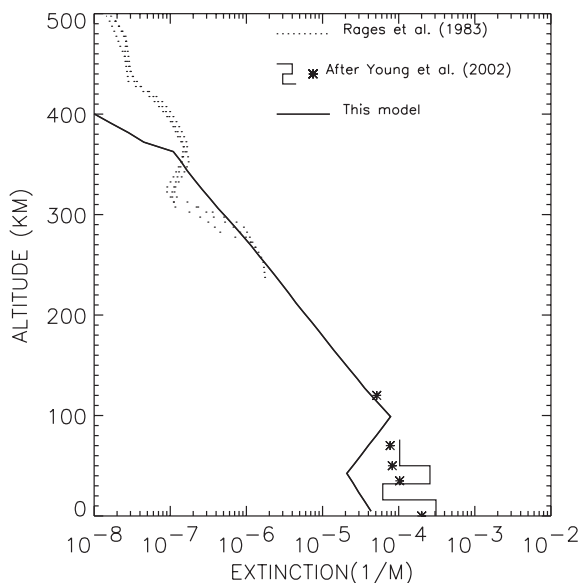


Fig. 6. Haze extinction profile in the case of extinction inversion, shown with the extinction profile derived by Rages and Pollack (1983), and values adapted from Young et al. (2002).

not a one-dimensional world, and previous work has shown that Titan's vertical haze profile is not fully consistent with the simple microphysical solution in the troposphere (e.g. Young et al., 2002). Condensation may occur and modify the vertical structure. However, it remains difficult to explain how the gap is produced. A rainout would decrease particle density due to increasing settle speed. But one must account for a simultaneous increase in cross sections due to condensation, which would leave a small effect on extinction.

Fig. 6 shows the new type of profile with extinction inversion in the low stratosphere. Fig. 7 shows the corresponding fit which can be obtained. The fit is globally good, and this time, the $0.88 \mu\text{m}$ band albedo has the correct albedo. The parameters used to obtain this fit are displayed in Table 1—right column.

5. Discussion and comparison

5.1. The vertical structure

Previous work has suggested that the haze is removed or thinned at low altitude. Young et al. (2002) study in detail the $0.88 \mu\text{m}$ methane band to produce a 3-D map of the haze. They show a global change in the extinction profile scale height around 100 km (Fig. 5). They also show that a gap in extinction coefficient, including an inversion, occurs around 40 km, for latitudes north of 15°S . Griffith et al. (1991) also indicate that a haze extinction profile chopped below 70 km is better in fitting their data than a haze profile which follows the microphysical solution down to the

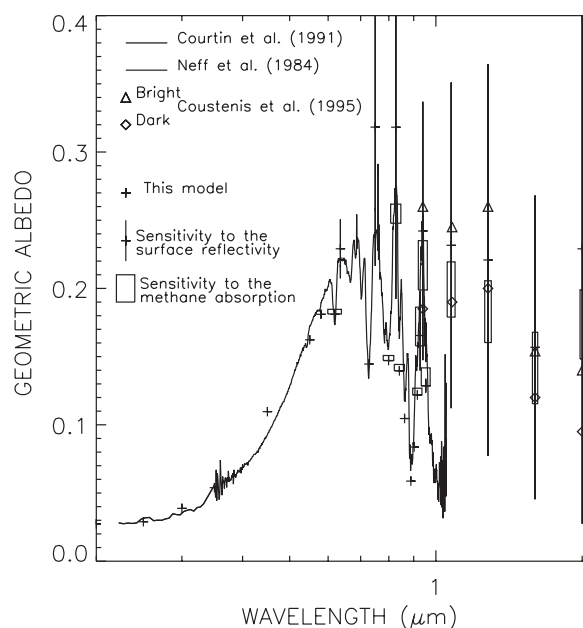


Fig. 7. As Fig. 2 except that the fit is for our preferred case with extinction inversion (see Table 1).

ground. Chanover et al. (2003) also find that their data at $1 \mu\text{m}$ is consistent with haze reduction below 60–70 km. The coincidence between the altitude where cut-off is needed in this work, in Young et al. (2002), Chanover et al. (2003) and also, in Griffith et al. (1991) may not be fortuitous. This conclusion that haze structure differs from a simple microphysical solution arises from different constraints in each of these studies. However, the exact detail of the vertical haze structure remains unknown.

We propose a simple vertical haze structure that meets all the constraints we know about haze. The extinction coefficient must match Rages and Pollack (1983) profiles above 200 km. It corresponds to a main haze production rate of about $7 \times 10^{-14} \text{ kg m}^{-2} \text{ s}^{-1}$. Moreover, the apparent size of the aggregates is constrained to be between 0.2 and $0.5 \mu\text{m}$. In the stratosphere, down to 100 km, the haze extinction follows the atmospheric scale height. Below a certain altitude the haze changes its scale height. We simply exponentially decrease the haze opacity below about 100 km. Fig. 6 gives an overview of the haze structure derived from this work.

5.2. Spectral behavior of haze opacity in near-infrared

The consistency of all these works in giving the behavior of the total optical depth in near-infrared is remarkable. Griffith et al. (1991), Gibbard et al. (1999) and Young et al. (2002) give helpful constraints on the integrated optical depth between 0.9 and $2.0 \mu\text{m}$ (Fig. 1). Neither Gibbard et al. nor Young et al. invoke stratospheric clouds to explain their data. Griffith et al. only need optically thin clouds in

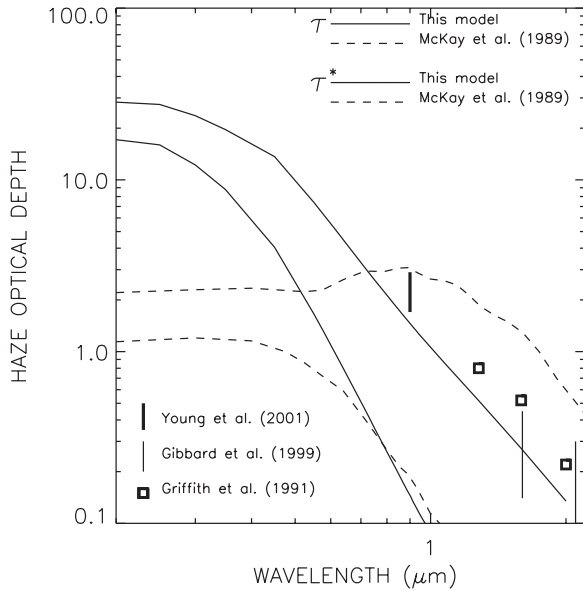


Fig. 8. The integrated haze optical depth as a function of wavelength for McKay et al. (1989) models of spherical aerosols (dashed thick line) and for the fractal aggregates model presented in this paper (inversion case). The thin continuous line corresponds to the effective haze opacity for the fractal aerosols haze. Same values as in Fig. 1 are also plotted for comparison.

the troposphere. The spectral behavior of the haze opacity between 0.9 and 2.0 is consistent with haze only, supporting the fact that clouds are not optically thick.

Fig. 8 shows the haze opacity and the effective haze opacity given by the model as a function of wavelength. The total haze opacity is slightly lower than those deduced from observations. Two facts explain this difference. First, the values retrieved by the different authors depend on the aerosols optical properties used in their works. Secondly, Fig. 5 shows that haze extinction deduced by Young et al. (2002) increases in the low troposphere. At these altitudes, aerosols do not strongly contribute to the global albedo that we have studied, except when looking in detail in the near-infrared methane bands. On the other hand, they contribute to the total opacity which is deduced from the methane windows. Our model could include an increase in extinction below about 40 km without changing the albedo. This would adjust the value of the total opacity without a change in the fit of the geometric albedo.

5.3. Surface features in visible

Observation shows that surface features may be seen through haze and methane at wavelengths as short as 0.55 μm (Smith et al., 1996; Lemmon et al., 2002). An important issue for this model, is to check that it is consistent with this fact. Fig. 7 already suggests that it is the case, but we display here more detailed arguments. We simply compute the relative difference

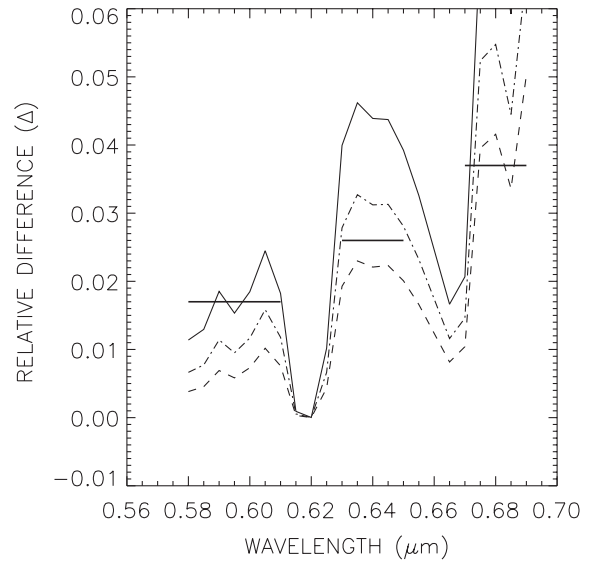


Fig. 9. Relative difference $\Delta = 2 \times (I_{\text{bright}} - I_{\text{dark}}) / (I_{\text{bright}} + I_{\text{dark}})$ on Titan’s reflectivity, at the center of the planet, and above bright and dark terrain, as a function of wavelength. Three curves show the results of the model obtained with a dark surface reflectivity at 0 and a bright surface reflectivity at 0.1 (dashed line), 0.15 (dot-dashed line) and 0.2 (continue line). The three horizontal lines are the observations derived from Lemmon et al. (2002).

$\Delta = 2 \times (I_{\text{bright}} - I_{\text{dark}}) / (I_{\text{bright}} + I_{\text{dark}})$ of the geometric albedo for a “dark” and “bright” surface reflectivity, and compare it to the observations cited above. Here, Δ is simply twice the contrast.

Because we do not know which is the actual “dark” and “bright” surface reflectivity, we just seek for the “bright” and “dark” contrast which best fits observations. Methane extinction between 0.58 and 0.8 μm is taken from Karkoschka (1994).

Fig. 9 shows Δ as a function of wavelength for 3 different surface contrasts. Dark terrain albedo is set to 0 whereas bright terrain albedo is set to 0.1, 0.15 and 0.2. This shows that realistic surface albedo contrasts (compared to other icy satellites, for instance) are able to be seen through the haze in our model. This plot also suggest that the reflectivity difference decreases from 0.2 to 0.1 within the spectral interval. However, we draw no firm conclusion from this last point since too many unknowns remain.

Fig. 10 shows the variation of Δ from the limb to the center of Titan’s disk at 0.673 μm. Smith et al. (1996) present a partial surface map based on 7 Hubble Space Telescope images at this wavelength—here we have extracted the surface contrasts from these images (HST program GO-5508) and plotted the range of pixel-to-pixel contrasts as a function of emission angle. It can be seen that the variation is quite consistent with our model, although note that the regions sampled in the images do not include the darkest terrains on Titan (trailing hemisphere), so the contrast plotted (~ 0.02) is less than might be expected considering a true

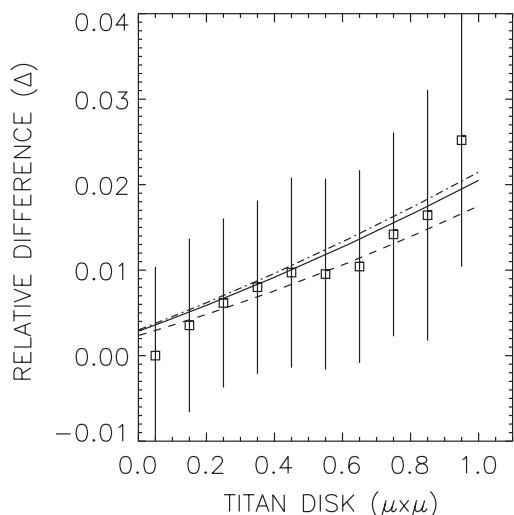


Fig. 10. The relative difference $\Delta = 2 \times (I_{\text{bright}} - I_{\text{dark}}) / (I_{\text{bright}} + I_{\text{dark}})$ on Titan's reflectivity, at $\lambda = 0.673 \mu\text{m}$, as a function of distance to the planet centre. $\mu^2 = 1$ corresponds to the center and $\mu^2 = 0$ corresponds to the limb. Dark and bright reflectivity are taken to 0 and 0.06. The three lines are for wavelengths $\lambda = 0.670 \mu\text{m}$ (dashed), $0.675 \mu\text{m}$ (dot-dashed) and $0.680 \mu\text{m}$ (continue) which corresponds to methane extinction $k = 1.2 \times 10^{-1} \text{ km-am}^{-1}$, $k = 1.8 \times 10^{-2} \text{ km-am}^{-1}$ and $k = 2 \times 10^{-2} \text{ km-am}^{-1}$, respectively. The squares with error bars are observation derived from Smith et al. (1996). Note that for this data, "dark" values are not truly taken from a dark terrain—which was not available in Smith et al. (1996) observations—but rather from a medium terrain. On the other hand, the "bright" values are taken for a true bright area. This explains the smaller contrast (0.06) than those used in Fig. 9.

light–dark difference. Our model fit, generated with a difference in surface albedo of 0.06, agrees reasonably well. The spatially-resolved disk-centre spectra reported in Lemmon et al. (2002) do sample the bright and dark regions and show a contrast of (~ 0.04)—consistent with our model and surface reflectivity difference of 0.1–0.2. These values are consistent with estimates done elsewhere (Lorenz and Lunine, 1997, and more recently by Lemmon et al., 2002).

Clearly, the haze opacity assumed here allows moderate surface contrast (that is significantly smaller than the extreme contrast as 0 and 1 for dark and bright reflectivity) to appear in the geometric albedo observation, as pointed by other authors. Haze opacity in our model decreases from 5.1 to 3.3 for wavelengths between $\lambda = 0.6$ and $0.68 \mu\text{m}$.

6. Conclusion

We have developed an analytic model of fractal haze microphysics on Titan. We have compared this model to the detailed microphysical model of Cabane et al. (1993) and have used it to fit the geometric albedo of Titan. Based on these comparisons we draw the following conclusions:

(1) The analytical fractal model of Titan's haze that we have developed provides a quick solution for modeling. We

have used microphysical equations (McKay et al., 1989) adapted to fractal aggregates (Cabane et al., 1993). The results match the output of a reference model (Cabane et al., 1993; Rannou et al., 1997).

(2) To fit the geometric albedo with the model of fractal aerosols, we need to introduce a transition in the haze layer somewhere above 80 km. This transition consists in imposing a reduction of the extinction coefficient below a given level. We show that inversion of extinction profile is necessary to fit all the spectrum. Similar transition has already been reported by Young et al. (2002) and Chanover et al. (2003). Tomasko et al. (1997) have also used a complete removal of the haze extinction below 88 km, and added a bright cloud below, to fit the geometric albedo. The physical origin of this transition is not explained in this work. We believe that it is due to interactions with the dynamics and does not result from a purely 1 dimensional process.

(3) We propose a simple vertical haze profile for the main haze which accounts for several known constraints. This profile is represented in Fig. 5. The model is then able to match several important data:

- It bridges the Rages and Pollack (1983) extinction profiles above 250 km, derived from large phase angle photometry, and the Young et al. (2002) extinction profiles from analysis of near-infrared images of Titan.
- It gives a value for the total haze optical depth which is consistent with the composite profile built from Griffith et al. (1991), Gibbard et al. (1999) and Young et al. (2002) values. This also ensures that in our model, the haze is transparent in the near-infrared.
- This haze is also consistent with bright and dark albedo contrasts at visible wave-lengths.
- The haze height scale which is imposed by Rages and Pollack (1983) and Young et al. (2002) is consistent with a weak eddy diffusion or no diffusion at all.

(4) The observed spectral behavior of total opacity in near-infrared suggests that haze is the major source of opacity, aside from gaseous species. If clouds are present in stratosphere, they must be thin ($\tau \simeq 1$ and effective opacity $\tau^* \ll 1$).

(5) For the haze and aerosols characteristic, we get that the production rate must be close to $7 \times 10^{-14} \text{ kg m}^{-2} \text{ s}^{-1}$. This constraint is essentially due to observation of limb photometry and is quite robust. Monomer radius cannot be larger than $\simeq 75 \text{ nm}$. On the other hand, monomer radius may be as small as 40 nm. Table 1 (right column) shows our preferred parameters.

(6) This haze model gives a realistic overall structure of Titan haze. This vertical structure is retrieved from the geometric albedo data. It mainly represents the latitudes between about 60°S and 60°N , and thus ignores anomalous polar features.

Appendix A. Microphysical 1D-model in fractal version

A.1. The principle and the equations: sedimentation and coagulation

In this part, we discuss the way the microphysical laws have been adapted to the growth and the settling of fractal aggregates. We follow the approach of McKay et al. (1989). The equations that we use are adapted from the equations of the microphysics of aerosols which may be found in Fuchs (1964) or in Pruppacher and Klett (1978). However, to account for the fractal structure of the aggregates, we modify the equations following Cabane et al. (1993). The basic idea is simple and has also been used by Tomasko et al. (1997). The microphysical laws are written for spheres, using their radius. However, depending on the physical process that is involved, this radius either comes from the mass of the particle ($m = 4/3\pi\rho r^3$) or from its surface ($S = \pi r^2$), where ρ is the density of the bulk matter. Mass is involved, for example, in the thermal speed and in the sedimentation speed through the weight. Surface is involved, for example, in the coagulation rates or in the sedimentation speed through the drag force. For fractal aggregates of spheres, the mass is N times the mass of one monomer; $m = N \times 4/3\pi\rho r_m^3$. The apparent surface of the fractal aggregate is $S = N^{1/D}\pi r_m^2$. Here, D is the fractal dimension of the aggregate and r_m is the radius of the monomers. Then replacing the mass or the surface of fractal aggregates in the microphysical laws yields a dependence on N , D and r_m instead of r only.

The continuity equation is the first equation of the set. It links the number of aerosols and the settling speed at a given level to the cumulative production rate above this level.

$$-nv \frac{4}{3} \pi \rho N = \int_z^\infty \frac{q(z)}{r_m^3} dz = \frac{C(z)}{r_m^3}, \quad (\text{A.1})$$

where v is the settling velocity of the particle, n is the particle number density, ρ is the bulk density of the particle material, $q(z)$ is the local production rate, and $C(z)$ is the column production rate above the altitude z . The production profile of the haze is known to be located in a region with a vertical extent that is comparable to the atmospheric scale height. We have used a gaussian profile in pressure, located around 1 mbar (400 km) and having a thickness of 0.3 mbar (about one scale height). In this model, it is assumed that only coagulation affects the number of particles, and then, the equation for the flux of particles (the second equation of the set) can be written as (Toon et al., 1980; McKay et al., 1989):

$$\frac{d(nv)}{dz} = -Kn^2. \quad (\text{A.2})$$

The coagulation kernel and the settle speed are given for fractal aggregates as (Cabane et al., 1993) if $\lambda/r \gg 1$, we

have

$$K = \left[8 \left(\frac{3kT}{\rho} \right)^{1/2} r_m^{1/2} \right] N^{(4-D)/2D} = a' N^{(4-D)/2D} \quad (\text{A.3})$$

and

$$v = - \left[\frac{\rho g}{2n_a} \left(\frac{\pi}{2m_a kT} \right)^{3/2} r_m \right] N^{(D-2)/D} = -b' N^{(D-2)/D}, \quad (\text{A.4})$$

where T is the temperature, k is Boltzmann's constant, η is the atmosphere viscosity, g is gravity, n_a and m_a are the atmospheric number density and mean molecular weight, respectively. As the particles settle down in the atmosphere, the condition $\lambda/r \gg 1$ breaks down, and the true settling velocity and coagulation coefficient become, in the case $\lambda/r \ll 1$:

$$K = \left[8 \frac{kT}{3\eta} N^{(D-4)/2D} \right] N^{(4-D)/2D} = a' N^{(4-D)/2D} \quad (\text{A.5})$$

and

$$v = - \left[\frac{2\rho g}{9\eta} N^{1/D} r_m^2 \right] N^{(D-2)/D} = -b' N^{(D-2)/D}. \quad (\text{A.6})$$

In these equations we have cast the sedimentation speed and the coagulation kernel with factors a' and b' , defined as in McKay et al. (1989). For intermediate cases, functions depending on $Kn = \lambda/r$ depart from the molecular regime ($\lambda/r \gg 1$) to smoothly fit the hydrodynamical regime ($\lambda/r < 1$). For both the settling speed and the coagulation kernel, we use empirical Cunningham's corrections (Fuchs, 1964). The settling speed is written as $v = v_{\text{Hydro}} \times (1.0 + 1.257Kn + 0.4Kn \times \exp(-1.1/Kn))$ which gives the correct settling speed over all the Knudsen number range. Equivalently, the coagulation kernel is given as $K = K_{\text{Hydro}} \times \beta$ where

$$\beta \simeq \frac{1}{r/(r + \delta/\sqrt{2}) + \pi l_B/2\sqrt{2}r} \quad (\text{A.7})$$

is valid whatever the Knudsen number. Here, $\delta = (1/6rl_B)((2r + l_B)^3 - (4r^2 + l_B^2)^{3/2}) - 2r$, l_B is the aerosols mean free path and r is the aerosols apparent radius, that is $r = N^{1/D}r_m$.

To take into account the effect of the coulomb repulsion, we correct the coagulation coefficient K by a factor ε . It depends on the size of the aerosols which coagulate and the electric charge χ . We assume, following Borucki et al. (1987) that the electric charge is proportional with the radius of the aerosols, then we set ε as following (Fuchs, 1964; Cabane et al., 1993):

$$\varepsilon = \frac{(n_e N^{1/D} r_m)^2}{2kTN^{1/3} r_m}. \quad (\text{A.8})$$

Solving the new set of equations (Eqs. (A.3), (A.4), (A.8) and (12)) gives

$$\frac{dN^{(7D-12)/2D}}{dz} = -\frac{3}{4\pi\rho b'} \left(\frac{7D-12}{2D} \right) \times \left[\frac{a'C'(z)}{b'} + N^{(3D-8)/2D} \frac{q'(z)}{n(z)} \right], \quad (\text{A.9})$$

where $C'(z) = C(z)/r_m^3$ and $q'(z) = q(z)/r_m^3$, that is, the amount of matter counted as the number of monomers. One can check that if $D = 3$, the above equation becomes equivalent to Eq. (A.4) in McKay et al. (1989). This equation is integrated stepwise down the atmosphere for N as a function of altitude grid, knowing the fractal dimension (set to $D = 2$) and the monomer radius r_m .

A.2. The conceptual approach and equations for eddy diffusion

The equations above take into account the sedimentation and the coagulation. The solution is found solving numerically Eq. (A.9). McKay et al. (1989) neglected the effects of dynamics (generally represented by some eddy diffusion). This was acceptable because their spherical particles are large ($0.4 \mu\text{m}$) and fall rapidly. However, because the settling speed of fractal aggregates is much slower than for equivalent spheres, the dynamics will affect the vertical structure of the haze to a larger extent. The eddy diffusion is a term given as the second derivative of the aerosol mixing ratio, $\partial n/\partial t = -\partial/\partial z(K_D n_a \partial(m(z)/n_a)/\partial z)$, where $m(z)$ is the haze mass per cubic meter of atmosphere, and K_D is the eddy diffusion coefficient. Thus, the diffusion term at a given level v depends on the two adjacent levels $v - 1$ and $v + 1$. From this, we can see that it is not easy to solve a simple differential equation step by step, to get the aerosol size and number density.

To account for eddy diffusion within the framework of our semi-analytical approach, we proceed iteratively. For a given step of the iteration, we evaluate the eddy diffusion flux $\Phi = -K_D n_a \partial(m(z)/n_a)/\partial z$ based on the microphysical solution we have computed. Then we redo the computation of the haze properties, but we correct the settling speed by adding, at each level, an equivalent speed that accounts for the transport by diffusion. At each level, knowing the size and the number of the current haze properties, the diffusion speed is chosen to agree with the diffusion flux previously computed. The purpose is to get a solution for which the sedimentation mass flux plus the eddy diffusion mass flux is equals to the production rate.

The convergence of this algorithm directly depends on the value of the diffusion coefficient. For low eddy diffusion coefficients, the convergence process may be stopped after 5 iterations. For larger values, 20–100 iterations may be needed. There exists a limit beyond which no stable convergence is reached.

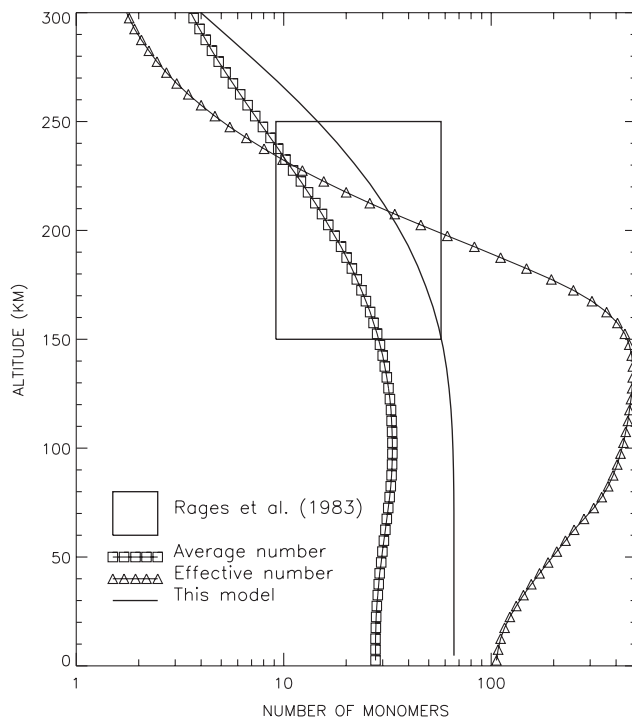


Fig. 11. Comparison between Cabane et al. (1993) model and our model. We compare the number of monomers per aggregates as a function of the altitude. The continuous line is for our model, the linked squares are the average monomer number and the linked triangles are the effective monomer number (see text for details) computed from Cabane et al. (1993). The box between 150 and 200 km gives the constraint given by Rages and Pollack (1983) on the effective radius ($0.2 \mu\text{m} < R < 0.5 \mu\text{m}$).

A.3. Performance of the microphysical code

In this part, we compare our model to the Cabane et al. (1992, 1993) eulerian model. The 1-D Cabane model solves the microphysics equations for an aerosol distribution that is fully described in the radius and altitude dimensions. The complexity of interactions between aerosols of different size are taken into account, as well as the vertical transport through sedimentation and eddy diffusion of the full distribution. For the comparison, we especially focus on the optical properties computed for the atmosphere that must be representative. We compare a distribution and the extinction vertical profile given by the eulerian model with well defined parameters (production rate and production altitude, aerosol charging) and the corresponding results for our model.

Fig. 11 shows the average monomer number per aggregate as a function of altitude for the eulerian model and for our model. We define the average monomer number $\langle N \rangle$. We also plot the extinction effective monomer number $\langle N \rangle_e$. The number $\langle N \rangle$ is the most relevant quantity for comparing two microphysical models, but we prefer to focus on the optical properties. If we set exactly the same input parameters, both model give exactly the same value of $\langle N \rangle$, excepted at low altitude. The decrease in the effective num-

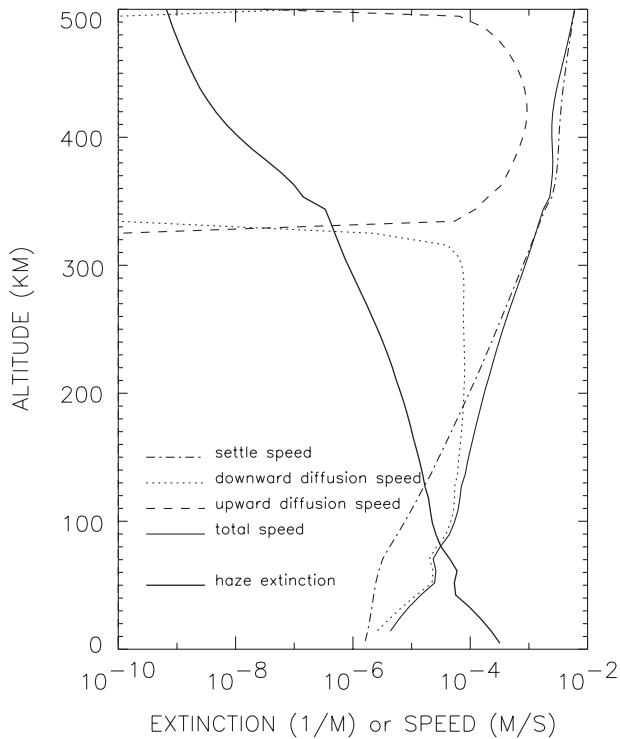


Fig. 12. Comparison between Cabane et al. (1993) model and our model: We plot the extinction coefficient (m^{-1}) for our model (thin continuous line) and for Cabane et al. (1993) model (triangles). The gross aerosol speed is given by the thick solid line (m/s) and is split into two terms; the sedimentation speed which dominates at high altitude (dotted line) and the diffusion speed which dominates at low altitude (dotted line; downward speed, dashed line: upward speed).

ber of monomer $\langle N \rangle$ below 100 km in the reference model is due the fact that for small Knudsen numbers, larger aggregates fall faster. This produces a relative impoverishment in large particles, compared to smaller ones. This effect obviously cannot be reproduced in our model. Fig. 11, shows our model results with a charging rate set to $25e^- \mu\text{m}^{-1}$ instead of $30e^- \mu\text{m}^{-1}$. This produces larger aerosols that are in better agreement with the effective number (based on extinction) of monomers in the reference model. This allows us to compare optical properties between the two models.

Fig. 12 shows vertical profiles of extinction for this model. On this figure, we have also plotted the sedimentation flux (thin continuous line), the eddy diffusion flux (dotted and dashed thin lines for downward and upward fluxes), and the total flux (heavy continuous line). Our model gives a very good match to the eulerian model result for the extinction profile, and many specific features of the vertical profile are also well reproduced. The effective speed profile (sedimentation + diffusion) produces a round profile above 100 km that is due to the diffusion. Sedimentation alone would produce a straight profile because the sedimentation speed is the same whatever the aggregate size (for $D = 2$). There is no relative acceleration due to the increasing size of particles.

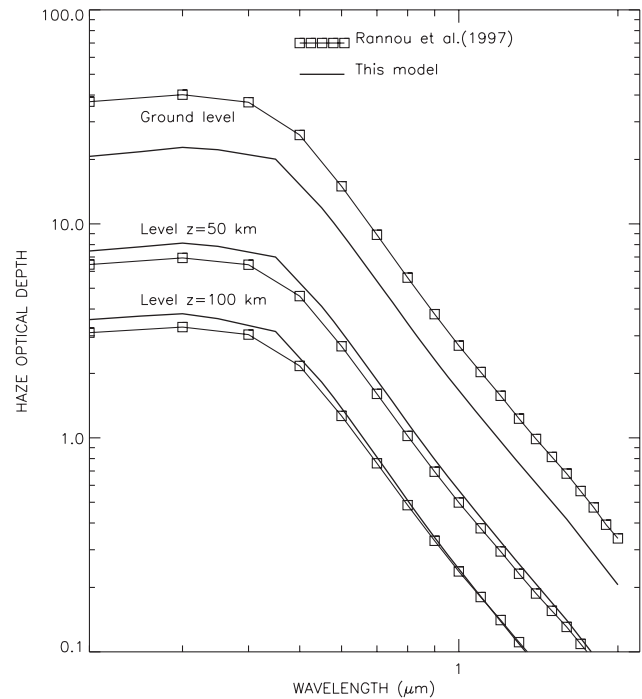


Fig. 13. The haze optical depth as a function of wavelength for the reference model (thick lines) and for our model (thin lines). From top to bottom, the coupled sets of lines are for opacity at the ground, at 50 km and at 100 km.

Fig. 13 shows the haze optical depth as a function of the wavelength for a haze distribution from the eulerian model, and for our model. The two models match well for altitudes above 50 km. In the troposphere, opacity seems to be underestimated in our model. This is probably due to the segregation effects in the hydrodynamics regime mentioned above. As can be seen in Fig. 13, the spectral behavior of the opacity is also well reproduced. The conclusion of this comparison is that we believe that our model gives the same relevant results compared to the reference model, regarding microphysical results as well as optical results. This fully validates the use of this model for the study that we perform in this paper.

References

- Borucki, W.J., Levin, Z., Whitten, R.C., Keese, R.G., Capone, L.A., Summers, A.L., Toon, O.B., Dubach, J., 1987. Predictions of the electrical conductivity and charging of the aerosols in Titan's atmosphere. *Icarus* 72, 604–622.
- Botet, R., Rannou, P., Cabane, M., 1997. Mean-field approximation of Mie scattering by a fractal aggregates. *Appl. Opt.* 36, 8791–8797.
- Cabane, M., Chassefière, E., Israel, G., 1992. Formation and growth of photo-chemical aerosols in Titan's atmosphere. *Icarus* 96, 176–189.
- Cabane, M., Rannou, P., Chassefière, E., Israel, G., 1993. Fractal aggregates in Titan's atmosphere. *Planet. Space Sci.* 41, 257–267.
- Chanover, N.J., Anderson, C.M., McKay, C.P., Rannou, P., Glenar, D.A., Hillman, J.J., Blass, W.E., 2003. Probing Titan's lower atmosphere with acousto-optic tuning. *Icarus*, 163, 150–163.

- Chassefière, E., Cabane, M., 1995. Two formation regions for Titan's haze: indirect clues and hypothesized chemical synthesis processes. *Planet. Space Sci.* 43, 91–103.
- Courtin, R., Wagener, R., McKay, C.P., Caldwell, J., Fricke, K.-H., Raulin, F., Brunton, P., 1991. UV spectroscopy of Titan's atmosphere, planetary organic chemistry and prebiological synthesis II. Interpretation of new IUE observations in the 220–335 nm range. *Icarus* 90, 43–56.
- Coustenis, A., Lellouch, E., Maillard, J.-P., McKay, C.P., 1995. Titan's surface: composition and variability from the near-infrared albedo. *Icarus* 118, 87–104.
- Fuchs, N.A., 1964. *The Mechanics of Aerosols*. Pergamon Press, Oxford.
- Gibbard, S.G., Macintosh, B., Gavel, D., Max, C.E., de Pater, I., Ghez, A.M., Young, E.F., McKay, C.P., 1999. Titan: high-resolution speckle images from the Keck telescope. *Icarus* 139, 189–201.
- Griffith, C.A., Owen, T., Wagener, R., 1991. Titan's surface and troposphere, investigated with ground-based, near-infrared observations. *Icarus* 93, 362–378.
- Israel, G., Cabane, M., Raulin, F., Chassefière, E., Boon, J.J., 1991. Aerosols in Titan's atmosphere: models, sampling techniques and chemical analysis. *Ann. Geophys.* 9, 1–13.
- Karkoschka, E., 1994. Spectrophotometry of the jovian planets and Titan at 300- to 1000 nm wavelength: the methane spectrum. *Icarus* 111, 174–192.
- Khare, B.N., Sagan, C., Arakawa, E.T., Suits, F., Calcott, T.A., Williams, M.W., 1984. Optical constants of organic tholins produced in a simulated Titanian atmosphere: from soft X-ray to microwave frequencies. *Icarus* 60, 127–137.
- Lemmon, M.T., Smith, P.H., Lorenz, R.D., 2002. Methane abundance on Titan, measured by the space telescope imaging spectrograph. *Icarus* 160, 375–385.
- Lorenz, R.D., Lunine, J.I., 1997. Titan's surface reviewed: the Nature of bright and dark terrain. *Planet. Space Sci.* 45, 981–992.
- McKay, C.P., Pollack, J.B., Courtin, R., 1989. The thermal structure of Titan's atmosphere. *Icarus* 80, 23–53.
- McKay, C.P., Coustenis, A., Samuelson, R.E., Lemmon, M.T., Lorenz, R.D., Cabane, M., Rannou, P., Drossart, P., 2001. Physical properties of the organic aerosols and clouds on Titan. *Planet. Space Sci.* 49, 79–99.
- Neff, J.S., Humm, D.C., Bergstrahl, J.T., Cochran, A.L., Cochran, W.D., Barker, E.S., Tull, R.G., 1984. Absolute spectrophotometry of Titan, Uranus and Neptune: 3,500–10,500 Å. *Icarus* 60, 221–235.
- Pollack, J.B., McKay, C.P., 1985. The impact of polar stratospheric clouds on the heating rates of the winter polar stratosphere. *J. Atmos. Sci.* 42, 245–262.
- Pruppacher, H.R., Klett, J.D., 1978. *Microphysics of Clouds and Precipitation*. Reidel Publishing Company, Dordrecht.
- Rages, K., Pollack, J.B., 1983. Vertical distribution of scattering haze in Titan's upper atmosphere. *Icarus* 55, 50–62.
- Rages, K., Pollack, J.B., Smith, P.H., 1983. Size estimate of Titan's aerosols based on Voyager high-phase-angle images. *J. Geophys. Res.* 88, 8721–8728.
- Rannou, P., Cabane, M., Chassefière, E., 1993. Growth of aerosols in Titan's atmosphere and related time scales: a stochastic approach. *Geophys. Res. Lett.* 20, 967–970.
- Rannou, P., Cabane, M., Chassefière, E., Botet, R., McKay, C.P., 1995. Titan's geometric albedo: role of the fractal structure of the aerosols. *Icarus* 111, 355–372.
- Rannou, P., Cabane, M., Chassefière, E., Botet, R., 1997. A new interpretation of scattered light measurements at Titan's limb. *J. Geophys. Res.* 102, 10,997–11,013.
- Rannou, P., McKay, C.P., Botet, R., Cabane, M., 1999. Semi-empirical model of absorption and scattering by isotropic fractal aggregates of spheres. *Planet. Space Sci.* 47, 385–396.
- Smith, P.H., Lemmon, M.T., Lorenz, R.D., Sromovsky, L.A., Caldwell, J.J., Allison, M.D., 1996. Titan's surface, revealed by HST imaging. *Icarus* 119, 336–349.
- Tomasko, M.G., Smith, P.H., 1982. Photometry and polarimetry of Titan: Pioneer 11 observations and their implications for aerosols properties. *Icarus* 51, 65–95.
- Tomasko, M.G., Lemmon, M., Roose, L.R., Smith, P.H., Eibl, A., West, R.A., 1997. Models of the penetration of sunlight into the atmosphere of Titan. *ESA SP-1177*, 345–358.
- Toon, O.B., Turco, R.P., Pollack, J.B., 1980. A physical model of Titan clouds. *Icarus* 43, 260–282.
- Toon, O.B., McKay, C.P., Griffith, C.A., Turco, R.P., 1992. A physical model of Titan aerosols. *Icarus* 95, 24–53.
- Toublanc, D., Parisot, J.P., Brillet, J., Gautier, D., Raulin, F., McKay, C.P., 1995. Photochemical modeling of Titan's atmosphere. *Icarus* 113, 2–26.
- West, R.A., 1991. Optical properties of aggregate particles whose outer diameter is comparable to the wavelength. *Appl. Opt.* 30, 5316–5324.
- West, R.A., Smith, P.H., 1991. Evidence for aggregate particles in the atmospheres of Titan and Jupiter. *Icarus* 90, 330–333.
- West, R.A., Lane, A.L., Hart, H., Simmons, K.E., Hord, C.W., Coffeen, D.L., Esposito, L.W., Sato, M., Pomphrey, R.B., 1983. Voyager 2 photopolarimeter observations of Titan. *J. Geophys. Res.* 88, 8699–8708.
- Young, E.F., Rannou, P., McKay, C.P., Griffith, C.A., Noll, K., 2002. A three dimensional map of Titan's tropospheric haze distribution based on HST imaging. *Astron. J.* 123-6, 3473–3486.
- Yung, Y.L., Allen, M., Pinto, J.P., 1984. Photochemistry of the atmosphere of Titan: comparison between model and observations. *Astrophys. J. Suppl. Ser.* 55, 465–506.